PNAS RESEARCH ARTICLE | NEUROSCIENCE

Differential nanoscale organization of excitatory synapses onto excitatory vs. inhibitory neurons

Poorna A. Dharmasri[a,b,c,1], Aaron D. Levy[a,c,1], and Thomas A. Blanpied[a,b,c,2]

Edited by Bernardo Sabatini, Harvard Medical School, Boston, MA; received September 18, 2023; accepted March 14, 2024

A key feature of excitatory synapses is the existence of subsynaptic protein nanoclusters (NCs) whose precise alignment across the cleft in a transsynaptic nanocolumn influences the strength of synaptic transmission. However, whether nanocolumn properties vary between excitatory synapses functioning in different cellular contexts is unknown. We used a combination of confocal and DNA-PAINT super-resolution microscopy to directly compare the organization of shared scaffold proteins at two important excitatory synapses—those forming onto excitatory principal neurons (Ex→Ex synapses) and those forming onto parvalbumin-expressing interneurons (Ex→PV synapses). As in Ex→Ex synapses, we find that in Ex→PV synapses, presynaptic Munc13-1 and postsynaptic PSD-95 both form NCs that demonstrate alignment, underscoring synaptic nanostructure and the transsynaptic nanocolumn as conserved organizational principles of excitatory synapses. Despite the general conservation of these features, we observed specific differences in the characteristics of pre- and postsynaptic Ex→PV nanostructure. Ex→PV synapses contained larger PSDs with fewer PSD-95 NCs when accounting for size than Ex→Ex synapses. Furthermore, the PSD-95 NCs were larger and denser. The identity of the postsynaptic cell was also represented in Munc13-1 organization, as Ex→PV synapses hosted larger Munc13-1 puncta that contained less dense but larger and more numerous Munc13-1 NCs. Moreover, we measured the spatial variability of transsynaptic alignment in these synapse types, revealing protein alignment in Ex→PV synapses over a distinct range of distances compared to Ex→Ex synapses. We conclude that while general principles of nanostructure and alignment are shared, cell-specific elements of nanodomain organization likely contribute to functional diversity of excitatory synapses.

nanocolumn | interneuron | PSD-95 | Munc13 | parvalbumin

Significance

Several properties of synaptic transmission are influenced by the transsynaptic alignment of key protein nanoscale assemblies. However, the extent to which protein organization within a synapse is unique across synapse types is not known. Using robustly quantitative DNA-PAINT imaging and several analysis approaches, we report that at excitatory synapses forming onto two different cell types, the general organizational features of core synaptic proteins are conserved. However, the identity of the postsynaptic neuron shapes transsynaptic relationships as well as specific nano-organizational properties within each cell. This suggests that retrograde specification of subsynaptic organization contributes to synaptic functional diversity. Understanding the rules of synapse nanodomain assembly, which themselves are cell-type specific, will be essential for illuminating brain network dynamics.

Many synaptic proteins are organized into subsynaptic nanoclusters (NCs) to enable their vital functions in information transmission (1). This is true of presynaptic release-related proteins such as Munc13-1, which forms NCs that mark synaptic vesicle release sites within the active zone (AZ), and whose density within NCs contributes to variability in probability of release (2–5). Similarly, postsynaptic scaffolds such as PSD-95 form NCs that influence glutamate receptor distribution (6–8), highlighting the importance of subsynaptic protein organization in setting cis-synaptic properties. The impact of nanostructure also extends across the synaptic cleft—For instance, Munc13-1 NCs also contribute to synaptic functions that arise from transsynaptic relationships, including the magnitude and variance of postsynaptic response amplitudes (9). These transsynaptic functional impacts likely arise because NCs can be aligned across the synapse to form the transsynaptic nanocolumn (10), a structural configuration that aligns release sites with glutamate receptors and thus strengthens the postsynaptic response to action potential-evoked neurotransmitter release (7, 10–13). Indeed, dispersal of AMPARs out of the nanocolumn and into the rest of the synapse is sufficient to greatly reduce the amplitude of action potential-evoked postsynaptic currents (14), underscoring the relationship between the nanocolumn and synaptic transmission.

Protein nanoclustering is a synapse architectural feature that has been observed with diverse imaging modalities in myriad preparations, including synaptosomes, dissociated cultures, ex vivo slices, and in vivo imaging (15–20). However, nanocolumn alignment has been less frequently measured. Nanocolumns of Unc13A and clustered receptors have been identified at the Drosophila neuromuscular junction (21), and alignment of RIM and $GABA_A$Rs has been reported in inhibitory synapses (22), suggesting that the nanocolumn is an evolutionarily old and widespread structure. Despite this, we lack an understanding of how nanocolumn architecture may vary, even between excitatory synapse types, leaving unresolved whether or which properties of the nanocolumn are conserved. The near ubiquity of core proteins, including Munc13-1 and PSD-95, at different excitatory synapse types suggests that their nanostructural relationship might be stereotyped.

Preprint Server: https://www.biorxiv.org/content/10.1101/2023.09.06.556279v1.

Author contributions: P.A.D., A.D.L., and T.A.B. designed research; P.A.D. and A.D.L. performed research; P.A.D. and A.D.L. contributed new reagents/analytic tools; P.A.D. and A.D.L. analyzed data; and P.A.D., A.D.L., and T.A.B. wrote the paper.

The authors declare no competing interest.

This article is a PNAS Direct Submission.

[1]P.A.D. and A.D.L. contributed equally to this work.

[2]To whom correspondence may be addressed. Email: TBlanpied@som.umaryland.edu.

This article contains supporting information online at https://www.pnas.org/lookup/suppl/doi:10.1073/pnas.2315379121/-/DCSupplemental.

Published April 16, 2024.

However, while core proteins are shared, different neuron types express distinct sets of synaptic receptors, adhesion proteins, and accessory proteins (23–25) that could modify the organization of core elements. Thus, cellular context may be a critical variable that alters nanocolumn properties, tuning alignment to support the physiological functions of a particular circuit.

Most explorations of excitatory synapse nanostructure have been conducted on glutamatergic synapses forming onto spiny, excitatory neurons. To test whether cellular context impacts nanostructure, we considered another particularly important excitatory synapse type, the afferent excitatory synapses onto parvalbumin-expressing hippocampal interneurons (PV-INs). Excitatory drive onto PV-INs mediates numerous critical aspects of cognition and pathology (26, 27), so understanding their synaptic molecular architecture is of utmost importance. Synapses onto PV-INs have also been documented as having higher release probability (28, 29) and generally larger EPSCs (30, 31), functional properties that are influenced by nanostructure (1). Further, PV-INs express a profile of proteins that is relatively consistent across brain regions (24) but differs from that of principal cells (32–34), making them an ideal candidate for testing the conservation of nanocolumn properties.

Here, we used confocal imaging and 3-dimensional DNA-PAINT (DNA-Points Accumulation for Imaging in Nanoscale Topography) super-resolution microscopy to investigate differences in protein spatial organization between excitatory synapses onto excitatory neurons and onto PV-INs. This direct, quantitative comparison revealed that the generalities of synaptic nanostructure and the nanocolumn are conserved between these two synapse types. However, postsynaptic cell identity was linked with the specific nanoscale organization of both postsynaptic and presynaptic proteins, as well as the transsynaptic spatial relationship between them. Our results underscore that while being generally conserved, subsynaptic nanostructure may represent an additional axis upon which synaptic transmission can be tuned to fit the needs of specific cells.

Results

Pre- and Postsynaptic Protein Abundance and Density Depend on Postsynaptic Cell Type. To measure protein organization at specific synapse types, we identified postsynaptic cells as either excitatory neurons or PV-INs in DIV21 dissociated rat hippocampal cultures by infecting with lentivirus expressing Enhanced GFP (EGFP) under a Calcium/calmodulin-dependent protein kinase II (CaMKII) promoter or by immunostaining for PV, respectively. The robust expression of either EGFP or PV throughout the soma and dendrites allowed clear delineation of expected cell morphologies: Compared to excitatory neurons, PV-INs tended to have larger somata and longer dendrites with a distinct, near-total absence of dendritic spines (35). All cells were also immunostained for presynaptic Munc13-1 and postsynaptic PSD-95 to identify afferent excitatory synapses forming onto either the excitatory neurons (Ex→Ex) or PV-INs (Ex→PV).

Ex→PV synapses qualitatively appeared larger and brighter than their Ex→Ex counterparts by confocal microscopy and had a "railroad track"-like organization, appearing in parallel along the dendrite (Fig. 1 *A* and *B*). To achieve an unbiased quantification of synapse properties, we built a semiautomated workflow centered around the puncta detection tool SynQuant ((36); *SI Appendix*, Fig. S1). Using this approach, we were able to quantify 40,751 and 26,627 synapses from 48 CaMKII-expressing neurons and 27 PV-INs, respectively, across three independent cultures.

We first quantified the total amount of PSD-95 at each synapse by measuring its integrated intensity, normalizing within each culture replicate to the mean value at Ex→Ex synapses. The cumulative distribution was right-shifted in PV-INs (Fig. 1 *C*, *Left*), indicating more PSD-95 per-synapse. As synaptic content can differ based on activity history, we tested whether cellular context influenced this shift. Ex→PV synapses still had a higher PSD-95 integrated intensity when averaged per-cell (Fig. 1 *C*, *Right*). The difference in integrated intensity could be due to either a change in synapse size or protein density, so we next quantified the area and mean intensity of PSD-95 puncta. We found that PSD-95 puncta were larger in Ex→PV synapses when analyzed per-synapse or per-cell (Fig. 1*D*). In contrast, while the mean intensity of PSD-95 in all Ex→PV synapses showed a small increase, the per-cell analysis indicated that this was not a significant difference (Fig. 1*E*). These results indicate that PV-INs have larger, but not denser, excitatory postsynapses than CaMKII-expressing excitatory neurons.

We next asked whether postsynaptic cell identity was associated with differences in the corresponding afferent AZ, identified with Munc13-1 immunostaining. The normalized integrated intensity and area of Munc13-1 puncta were each significantly larger at Ex→PV synapses (Fig. 1 *F* and *G*). Further, unlike for PSD-95, the normalized mean intensity of Munc13-1 was higher onto PV-INs (Fig. 1*H*), indicating a greater Munc13-1 density within these AZs. These data together demonstrate that postsynaptic cell identity helped establish both pre- and postsynaptic content of core excitatory synapse proteins. The differences in synapse size and Munc13-1 density between these synapse types suggest the potential for differential underlying nanoscale organization of core synaptic proteins.

PSD-95 Nanostructure Is Differentially Organized Depending on Postsynaptic Cell Identity. We next used 3D DNA-PAINT to measure whether protein nano-organization differs between Ex→Ex and Ex→PV synapses (Fig. 2 *A* and *B*), focusing first on the PSD. Our super-resolution data showed Ex→PV PSDs were nearly two times the volume of Ex→Ex PSDs (Fig. 2*C*), consistent with the larger puncta area detected with confocal imaging. As PSD-95 NC number scales with synapse size at Ex→Ex synapses (15), we predicted that Ex→PV PSDs would contain more PSD-95 NCs. To test this, we detected PSD-95 NCs using DBSCAN. We were surprised to see no difference in the average number of PSD-95 NCs per-synapse (Fig. 2*D*). This could be due to a different relationship between PSD size and NC number at Ex→PV synapses. While the rate at which NC number increases with PSD size is not different between the two synapse types, Ex→PV synapses notably have fewer PSD-95 NCs for a synapse of a given size (Fig. 2*E*). These results suggest that Ex→PV PSDs are not simply enlarged versions of Ex→Ex PSDs but differ in their nano-organizational principles.

To directly interrogate whether PSD-95 nanocluster properties differ between the two synapse types, we first quantified the spatial heterogeneity of PSD-95 within single synapses using a normalized autocorrelation analysis, as described previously (10, 14). The autocorrelation of PSD-95 at Ex→PV synapses was higher in magnitude over longer shift radii, predicting larger, denser PSD-95 NCs than in Ex→Ex synapses (Fig. 2*F*). Measuring the autoenrichment, which analyzes the normalized density of a protein surrounding its NC peak, showed both a higher peak density and broader distribution (Fig. 2*G*) and PSD-95 NC volume was ~75% larger at Ex→PV synapses (Fig. 2*H*), confirming the autocorrelation predictions. We wondered whether the larger PSD-95 NCs at Ex→PV synapses ensured that the same fraction of the PSD was occupied by PSD-95 NCs despite being fewer in number. We found instead that PSD-95 NCs occupied a smaller proportion of the PSD at Ex→PV synapses than at Ex→Ex synapses (Fig. 2*I*). Together, these data demonstrate that PSD-95, a core scaffold protein of excitatory synapses, is differentially organized depending on postsynaptic cell identity. The unique subsynaptic pattern

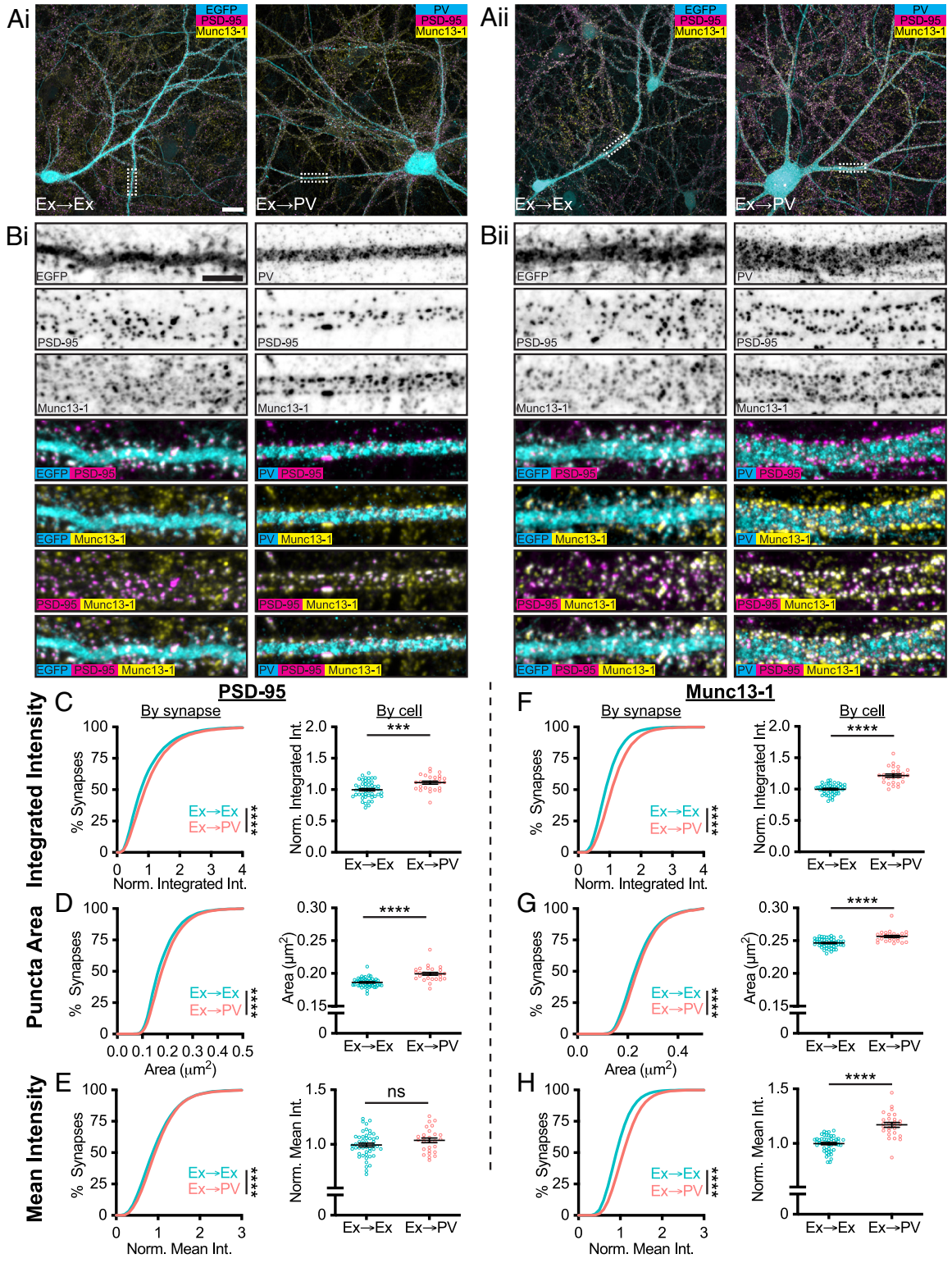

Fig. 1. Pre- and postsynaptic protein abundance and density depend on postsynaptic cell type. (*A*) Example neurons in dissociated hippocampal cultures from two independent cultures (*i* and *ii*). Excitatory synapses formed onto excitatory neurons (Ex→Ex) were identified by CaMKII promoter-driven EGFP expression (*A*, *i* and *ii*, *Left*), while excitatory synapses formed onto PV-INs (Ex→PV) were identified by PV staining (*A*, *i* and *ii*, *Right*). (Scale bar: 20 μm.) (*B*) Representative dendrite stretches from example cells above showing, from *Top* to *Bottom*, cell identifying marker, PSD-95 staining, and Munc13-1 staining, followed by two- and three-color merges indicating strong overlay of synaptic markers with one another and with dendritic spines/dendrites. (Scale bar: 5 μm.) (*C*–*H*) Analyses of synaptic protein content and puncta size. All data are presented on a per-synapse (*Left*) and per-cell (*Right*) basis. Per-synapse analyses, presented in cumulative distributions, represent the direct observations (Ex→Ex, n = 40,751 synapses; Ex→PV, n = 26,627 synapses; $P < 0.0001$ for all). Some CDFs are cut off at the 99th percentile for visibility. Per-cell analyses were conducted to account for cell-to-cell variability (Ex→Ex, n = 48 cells; Ex→PV, n = 27 cells; statistics below). Intensity measures are normalized within culture week to the average of the Ex→Ex group, and each cell is presented as a point along with the mean ± SEM, which is also reported below. (*C*) Ex→PV synapses contain more PSD-95 (per-cell: Ex→Ex, 1.00 ± 0.019; Ex→PV, 1.11 ± 0.023; $P = 0.0004$). (*D*) Ex→PV PSDs are larger than their Ex→Ex counterparts (per-cell: Ex→Ex, 0.19 ± 0.0010 μm^2; Ex→PV, 0.20 ± 0.0021 μm^2; $P < 0.0001$). (*E*) PSD-95 density is not different between synapse types when accounting for cell-to-cell variability (per-cell: Ex→Ex, 1.00 ± 0.017; Ex→PV, 1.04 ± 0.021; $P = 0.1281$). (*F*) Ex→PV synapses contain more Munc13-1 (per-cell: Ex→Ex, 1.00 ± 0.012; Ex→PV, 1.22 ± 0.025; $P < 0.0001$). (*G*) AZs are larger in Ex→PV synapses (per-cell: Ex→Ex, 0.25 ± 0.0010 μm^2; Ex→PV, 0.26 ± 0.0016 μm^2; $P < 0.0001$). (*H*) Ex→PV synapse AZs have a greater Munc13-1 density (per-cell: Ex→Ex, 1.00 ± 0.011; Ex→PV, 1.17 ± 0.022; $P < 0.0001$).

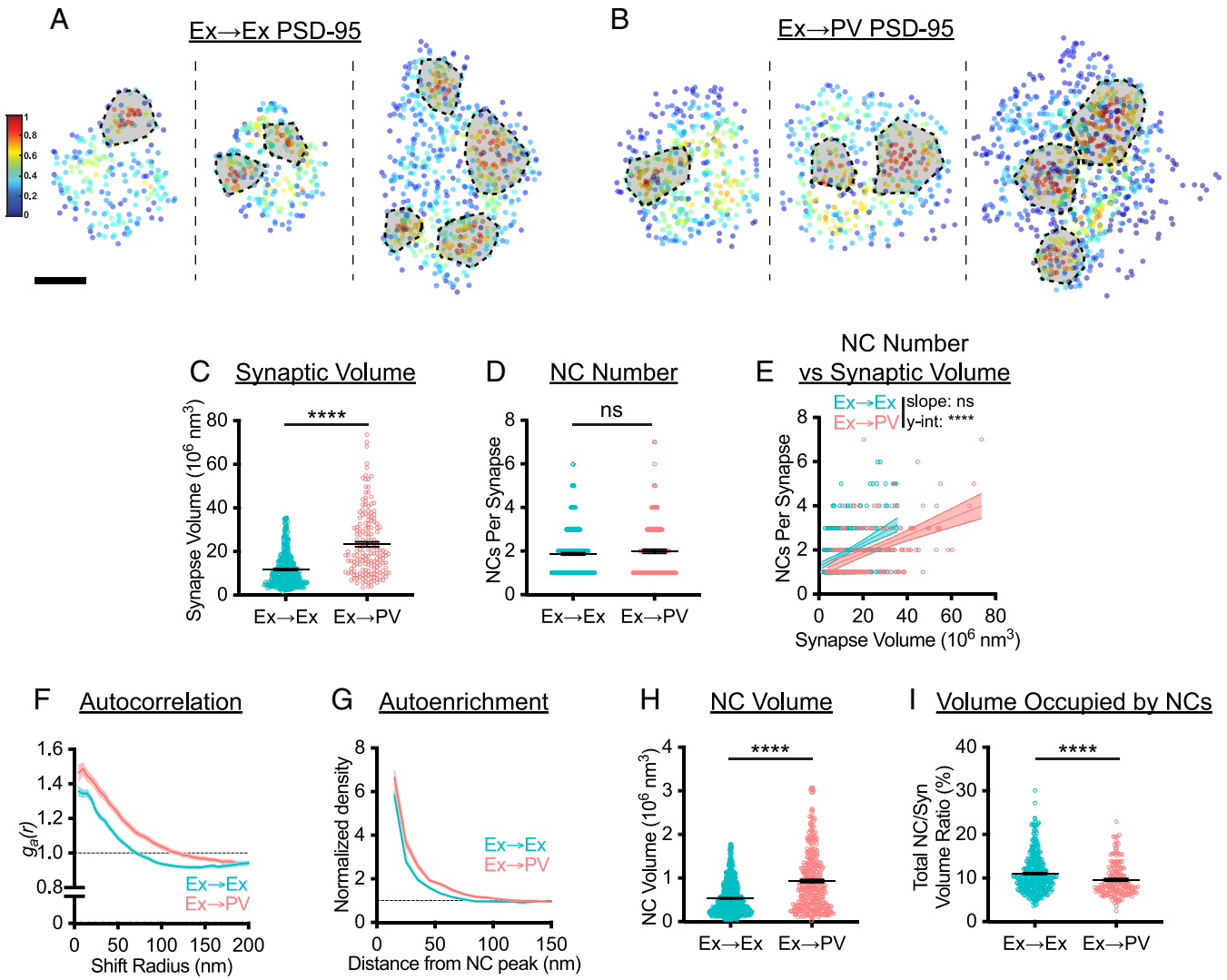

Fig. 2. PSD-95 nanostructure is differentially organized depending on postsynaptic cell identity. (*A* and *B*) Examples of 3D DNA-PAINT PSD-95 synaptic clusters from (*A*) Ex→Ex and (*B*) Ex→PV synapses. Heat maps indicate the peak density–normalized local density. Black-bordered shapes indicate detected NCs. (Scale bar: 100 nm.) Parentheticals below indicate mean ± SEM. (*C*) PSDs are larger at Ex→PV synapses (Ex→Ex, 11.76 ± 0.41 × 10^6 nm^3; Ex→PV, 23.32 ± 1.14 × 10^6 nm^3; $P < 0.0001$). (*D*) Both synapse types contain the same number of PSD-95 NCs on average (Ex→Ex, 1.87 ± 0.054 NCs/synapse; Ex→PV, 1.99 ± 0.092 NCs/synapse; $P = 0.4606$). (*E*) Ex→PV PSDs contain fewer NCs than expected when accounting for PSD size (Ex→Ex, slope: 0.053, y-intercept: 1.25, R^2: 0.17; Ex→PV, slope: 0.040, y-intercept: 1.058, R^2: 0.24. slope $P = 0.1009$, y-intercept $P < 0.0001$). (*F*) Autocorrelation predicts PSD-95 forms larger, denser NCs in PV cells. (*G*) The average Ex→PV PSD-95 NC has a denser and broader PSD-95 distribution. (*H*) PSD-95 NC volume is larger at Ex→PV synapses (Ex→Ex, 0.54 ± 0.014 × 10^6 nm^3; Ex→PV, 0.94 ± 0.038 × 10^6 nm^3; $P < 0.0001$). (*I*) Less synapse volume is occupied by PSD-95 NCs at Ex→PV synapses (Ex→Ex, 11.03 ± 0.23% volume; Ex→PV, 9.62 ± 0.29% volume; $P < 0.0001$). Parentheticals above for (*C*, *D*, *H*, and *I*) list means ± SEM. Data in *C*–*E* and *I* are individual synapses, and in *H* individual NCs, with lines at mean ± SEM. Data in *E* are plotted with line of best fit ± 95% CI. Data in *F* and *G* show a line connecting the mean of each bin ± SEM shading. For Ex→Ex, n = 372 synapses or 667 NCs; for Ex→PV, n = 168 synapses or 327 NCs throughout.

of PSD-95 may strengthen the retention of mobile glutamate receptors within these larger synapses (*Discussion*).

Postsynaptic Cell-Type Is Linked to AZ Nanostructure. Given the higher Munc13-1 density at Ex→PV synapses (Fig. 1*J*), we asked whether the postsynaptic cell identity impacted the afferent Munc13-1 nanoscale organization (Fig. 3 *A* and *B*). Consistent with our confocal imaging observations, Munc13-1 occupied a larger total volume at Ex→PV than at Ex→Ex synapses (Fig. 3*C*), suggestive of a larger AZ. Unlike PSD-95 NCs, Munc13-1 NCs were more numerous in Ex→PV synapses (Fig. 3*D*), suggesting that these AZs contain more release sites (an average of ~1 more per-synapse). In hippocampal CA1 pyramidal neuron synapses onto fast-spiking interneurons (FSINs), the number of Munc13-1 NCs scales with AZ size yet is strikingly variable even in AZs of similar size (3). We tested whether this was true both in Ex→PV and Ex→Ex synapses. The number of Munc13-1 NCs was similarly correlated with the size of the AZ in each synapse type (Fig. 3*E*). The spread of the data in the regression analysis is indicative of large variability in Munc13-1 NC number across similarly sized AZs. Agnostic to synapse size, the variability in NC number per-synapse was large but not different between groups (Ex→Ex: CV 0.58 vs. Ex→PV: CV 0.59). Together, these data are consistent with previous findings and suggest that postsynaptic cell identity can influence AZ size.

A closer look at Munc13-1 nanocluster properties revealed further postsynaptic cell type-dependent differences. Autocorrelation analysis of the Munc13-1 distribution in Ex→PV synapses showed a lower initial magnitude with a concomitant rightward shift in the middle portion of the curve (Fig. 3*F*), predicting larger, but less dense NCs than at Ex→Ex synapses. Consistent with these predictions, Munc13-1 NCs at Ex→PV synapses had higher local density at longer distances from the NC peak (Fig. 3*G*) and were larger (Fig. 3*H*) than those at Ex→Ex synapses. The combination

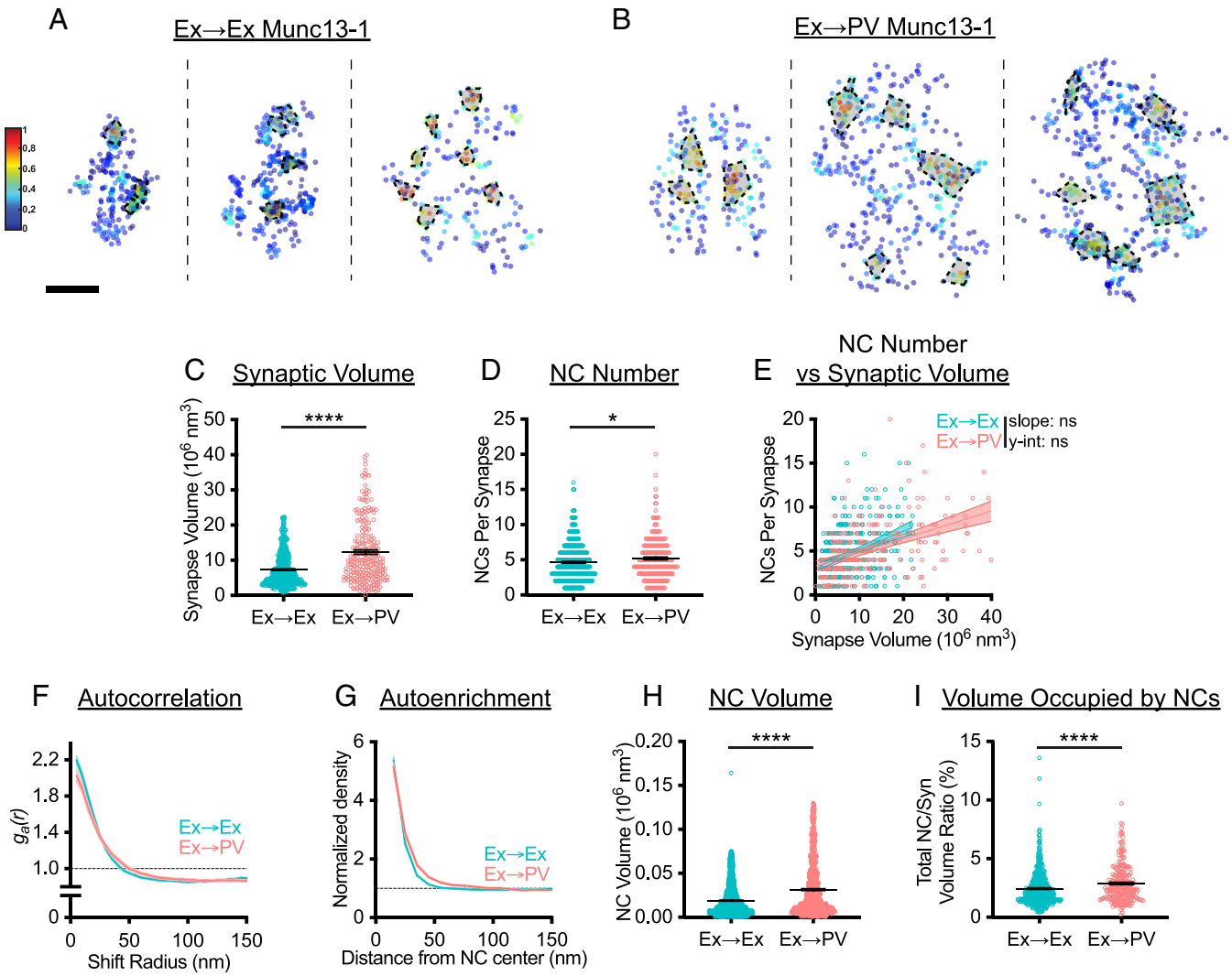

Fig. 3. Postsynaptic cell-type is linked to AZ nanostructure. (*A* and *B*) Examples of 3D DNA-PAINT Munc13-1 synaptic clusters from (*A*) Ex→Ex and (*B*) Ex→PV synapses. Heat maps indicate peak density–normalized local density. Black-bordered shapes indicate detected NCs. (Scale bar: 100 nm.) (*C*) Munc13-1 AZ clusters are larger in Ex→PV synapses (Ex→Ex, 7.31 ± 0.22 × 10^6 nm^3; Ex→PV, 12.34 ± 0.59 × 10^6 nm^3; $P < 0.0001$). (*D*) Ex→PV synapses contain more Munc13-1 NCs. (Ex→Ex, 4.63 ± 0.13 NCs/synapse; Ex→PV, 5.21 ± 0.20 NCs/synapse; $P = 0.0143$). (*E*) Munc13-1 NC number scales similarly with AZ size between synapse types (Ex→Ex, slope: 0.21, y-intercept: 3.10, R^2: 0.14; Ex→PV, slope: 0.16, y-intercept: 3.28, R^2: 0.21; slope $P = 0.1016$, y-intercept $P = 0.1887$). (*F*) Autocorrelation predicts Munc13-1 forms larger, less dense NCs at Ex→PV synapses. (*G*) The average Ex→PV Munc13-1 NC has a broader Munc13-1 distribution with lower central density. (*H*) Munc13-1 NC volume is larger at Ex→PV synapses (Ex→Ex, 0.019 ± 0.00042 × 10^6 nm^3; Ex→PV, 0.032 ± 0.00096 × 10^6 nm^3; $P < 0.0001$). (*I*) More of the synapse volume is occupied by Munc13-1 NCs in Ex→PV synapses (Ex→Ex, 2.45 ± 0.071% volume; Ex→PV, 2.89 ± 0.11 % volume; $P < 0.0001$). Parentheticals above for (*C*, *D*, *H*, and *I*) list means ± SEM. Data in *C*–*E* and *I* are individual synapses, and in *H* individual NCs, with lines at mean ± SEM. Data in *E* plotted with line of best fit ± 95% CI. Data in *F* and *G* show a line connecting the mean of each bin ± SEM shading. For Ex→Ex, n = 454 synapses or 1,839 NCs; for Ex→PV, n = 229 synapses or 1,046 NCs throughout.

of more numerous and larger Munc13-1 NCs at Ex→PV synapses resulted in a larger fraction of the AZ being occupied by these NCs (Fig. 3*I*). These data together demonstrate that the postsynaptic cell influences apposed AZ size as well as Munc13-1 NC volume and density, parameters which may affect synaptic vesicle docking, priming, or probability of release, which are high at Ex→PV synapses (28, 37–39).

Impact of Postsynaptic Cell-Type on Transsynaptic Alignment. In the prototypical Ex→Ex synapse, synaptic strength depends on the transsynaptic coordination of nanostructure (11, 14, 40). Given that in Ex→PV synapses more of the AZ is occupied by Munc13-1 NCs but less of the PSD is occupied by PSD-95 NCs (compare Figs. 2*I* and 3*I*), we predicted that transsynaptic alignment in Ex→PV synapses would be weaker. We first measured the distance between the nearest NC peaks of opposing proteins (Fig. 4 *A* and *B*). Consistent with larger synapses, in Ex→PV synapses, the peak of Munc13-1 NCs was slightly further away from the nearest identified PSD-95 NC peak, and vice versa (Fig. 4*C*), suggesting weaker alignment between release sites and postsynaptic scaffolds. However, while the NC peaks may be further apart, NCs, particularly of PSD-95, do not contain the majority of the scaffold protein (7), limiting the utility of the peak-to-peak analysis. We thus analyzed alignment with two additional approaches that consider protein distribution without relying on identifying NCs of each.

To dispense with NC identification entirely, we first used a cross-correlation analysis that reports the overall similarity of nanoscale protein distributions within the synapse (10). This showed a higher magnitude over shift radii up to 150 nm at Ex→PV synapses (Fig. 4*D*), consistent with stronger transsynaptic nanoscale alignment of Munc13-1 and PSD-95 overall. The increase in the width of the cross-correlation is consistent with the larger NCs found in Ex→PV synapses since in a synapse

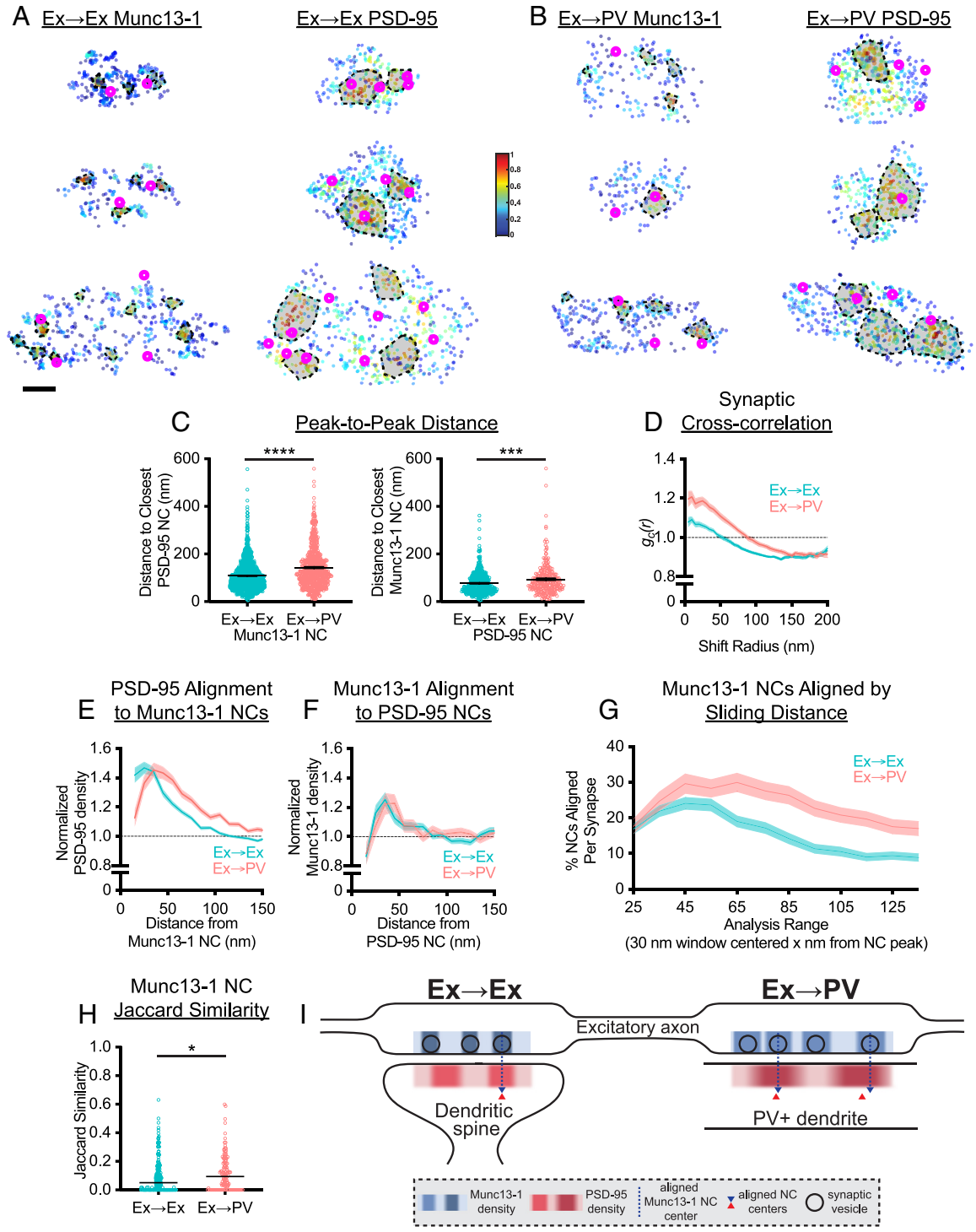

Fig. 4. Impact of postsynaptic cell-type on transsynaptic alignment. (*A* and *B*) Example 3D DNA-PAINT synapses from (*A*) Ex→Ex and (*B*) Ex→PV synapses. Magenta circles indicate centers of NCs of opposing protein, and the heat map indicates peak density–normalized local density of labeled protein. Each row is an individual synapse with corresponding AZ and PSD clusters in the indicated columns. (Scale bar: 100 nm.) (*C*) Munc13-1 and PSD-95 NC peaks are further from each other in Ex→PV synapses (mean ± SEM of Munc13-1 NC to closest PSD-95 NCs: Ex→Ex, 108.7 ± 1.90 nm, n = 1,141 NCs; Ex→PV, 142.9 ± 3.21 nm, n = 695 NCs; $P < 0.0001$. PSD-95 NC to closest Munc13-1 NCs: Ex→Ex, 77.09 ± 2.21 nm, n = 448 NCs; Ex→PV, 93.82 ± 4.28 nm, n = 246 NCs; $P = 0.0004$). (*D*) Synaptic cross-correlation indicates stronger transsynaptic alignment in Ex→PV synapses (Ex→Ex, n = 245 synapses; Ex→PV, n = 129 synapses). (*E*) The enrichment of PSD-95 density across from Munc13-1 NCs indicates an offset in nanocolumn alignment in Ex→PV synapses (Ex→Ex, n = 1,067 NCs; Ex→PV, n = 623 NCs). (*F*) The enrichment of Munc13-1 density across from PSD-95 NCs has a broader, rightward-skewed peak in Ex→PV synapses (Ex→Ex, n = 474 NCs; Ex→PV, n = 263 NCs). (*G*) Ex→PV synapse Munc13-1 NCs are aligned at a higher percentage over a broader range than their Ex→Ex counterparts (for *G*–*I*, Ex→Ex, n = 237 synapses; Ex→PV, n = 124 synapses). (*H*) Both Ex→Ex and Ex→PV synapses have diverse nanocolumn subtypes within a single synapse, indicated by the low Jaccard Similarity coefficient (JS). Ex→PV synapses have slightly more similarity between nanocolumns within a single synapse than Ex→Ex synapses (median JS: Ex→Ex, 0.05, n = 211 synapses; Ex→PV, 0.09, n = 113 synapses; $P = 0.011$). (*I*) Model of nanostructural differences between Ex→Ex and Ex→PV synapses. Compared to Ex→Ex synapses, Ex→PV synapses have larger Munc13-1 and PSD-95 synaptic areas, with larger and denser PSD-95 NCs and larger but less dense Munc13-1 NCs. The number of PSD-95 NCs is not different, though there is on average 1 additional Munc13-1 NC per-synapse. Transsynaptic alignment is intact in Ex→PV synapses, though Munc13-1 NCs are on average offset from the peak of PSD-95 density, but still aligned, resulting in different nanocolumn "types" at these synapses. Data in *C* are individual NCs with lines at mean ± SEM. Data in *D*–*G* show a line connecting mean of each bin ± SEM shading. Data in *H* are individual synapses with line at median.

displaying nanocolumn alignment, this would position more protein near opposing areas of high protein density, a fact not captured in the peak-to-peak distances.

To test alignment across from identified NCs of just one protein species, we measured the cross-enrichment, which is the normalized radial distribution of the opposing protein across from a given NC's peak. PSD-95 was strongly cross-enriched to Munc13-1 NC peaks, and vice versa, within both synapse types (Fig. 4 *E* and *F*), suggesting that despite larger and slightly broader spaced NCs, the overall relationship of transsynaptic spatial alignment is maintained in Ex→PV synapses. Along with the cross-correlation analysis, this confirms the presence of a conserved nanocolumn architecture between Ex→Ex and Ex→PV synapses.

Intriguingly, however, the cross-enrichment analyses revealed specific organizational differences between the two synapse types. The peak density of PSD-95 was shifted 10 to 20 nm further away from Munc13-1 NCs in Ex→PV synapses (Fig. 4*E*). The offset was also reflected in the cross-enrichment of Munc13-1 density to PSD-95 NCs, which was overall extremely similar between the two synapse types but showed a broader, rightward-skewed peak in Ex→PV synapses (Fig. 4*F*). These data suggest that nanocolumns within Ex→PV synapses comprise a slightly offset or perhaps annular transsynaptic organization when compared to Ex→Ex synapses. This is an important notion because the most widely considered working model of nanocolumn alignment is that cell adhesion molecules (CAMs) with discrete interactions across the cleft provide the basis for a stereotyped transcellular architecture. Since different cells and synapses express distinct subsets of CAMs that may interact with distinct molecular populations, this raises the possibility that the nanocolumn in different synapse types could be constructed with a consistent but unique structure. Thus, while nanocolumns exist in both synapses, Ex→PV synapses may contain different nanocolumn "subtypes" than Ex→Ex synapses.

To establish whether the unexpected shift in cross-enrichment in Ex→PV synapses indicated a single population of consistently structured nanocolumns or rather a broad distribution of nanocolumn subtypes, we developed analyses to examine the heterogeneity in alignment in the population of Munc13-1 NCs within the analyzed synapses. We determined the percentage of Munc13-1 NCs that were aligned per-synapse by testing whether each Munc13-1 NC was statistically enriched with PSD-95 or not within a specific radius. When we applied this measure using a radius of 60 nm as in previous work (10) and calculated the percent of aligned Munc13-1 NC per-synapse, the same percentage was aligned in each synapse type (*SI Appendix*, Fig. S2*A*). However, NCs are larger at Ex→PV synapses, and so to evaluate this relationship more systematically, we varied the width of the analysis range from 20 to 150 nm, calculating for each range the percent of Munc13-1 NCs per-synapse statistically aligned to PSD-95. The percentage of aligned Munc13-1 NCs was similar between Ex→Ex and Ex→PV synapses up to 100 nm away from the NC peak (*SI Appendix*, Fig. S2*B*). Given that the difference in the peak cross-enrichment to Munc13-1 NCs was observed within this distance (Fig. 4*E*), we probed for a specific distance at which Munc13-1 was enriched with PSD-95 using a sliding window of 30 nm for the analysis. This revealed different preferred distances for the two synapse types even within those first 100 nm; most Munc13-1 NC alignment occurred around 35 to 55 nm in Ex→Ex synapses, but in Ex→PV synapses maximal alignment occurred further away and across a wider range of distances (45 to 75 nm; Fig. 4*G*). Overall, these results are consistent with the idea that nanocolumn architecture is generally conserved, but that Ex→PV synapses host a wider distribution of nanocolumn subtypes than Ex→Ex synapses, presumably arising from engagement of their unique set of cleft-resident molecules.

If Ex→PV synapses as a population have more nanocolumn subtypes, it is possible that those subtypes occur in different synapse subpopulations or appear even within single synapses. To test this, we reanalyzed the data from Fig. 4*G* and for each synapse evaluated the similarity of its Munc13-1 NCs in terms of their PSD-95 enrichment profiles. For this, we calculated the Jaccard similarity coefficient (JS) for each pair of NCs in a synapse, which can range from 0 to 1, where 0 indicates no similarity in their PSD-95 enrichment profile, and 1 indicates an identical profile. Therefore, a synapse with high average JS would contain very similar nanocolumn subtypes, while one with low average JS would have high nanocolumn diversity. Overall, Ex→Ex and Ex→PV synapses both had low JS, indicating that both synapse types are composed of many nanocolumn subtypes within a single synapse (Fig. 4*H*). Ex→PV synapses on average did have slightly higher JS, suggesting that they have relatively more intrasynaptic nanocolumn similarity, though the median JS of 0.09 was still very low. Both the low JS and the difference between synapse types were maintained when synapses with JS = 0, i.e., those that lacked any similarity in PSD-95 enrichment profiles between Munc13-1 NC pairs, were removed from analysis, emphasizing these findings were not solely driven by synapses that have no similarity (*SI Appendix*, Fig. S2*C*). A possible explanation for this difference between synapse types is the higher number of Munc13-1 NCs in Ex→PV synapses. Packing in more of these relatively small NCs could result in a greater proportion of them experiencing a similar transsynaptic enrichment with PSD-95, which has even broader areas of elevated density in Ex→PV synapses. However, the JS in both synapse types was only very weakly dependent on NC number, indicating that this was largely not the case (*SI Appendix*, Fig. S2*D*). Further, the median Munc13-1 NC peak-to-peak distances were slightly higher for Ex→PV synapses as expected for their larger AZs (Fig. 3 *C* and *E*) but did not differ across increasing JS values (*SI Appendix*, Fig. S2*E*). Together with the data in Fig. 4*G*, these results confirm that while Ex→PV synapses can host a broader diversity of nanocolumn subtypes, Ex→Ex synapses have slightly more diversity of subtypes within a single synapse. More broadly, they emphasize that single synapses onto either cell-type can and often do contain multiple configurations of nanocolumn alignment.

Discussion

In this study, we used complementary intermediate-scale confocal imaging and single-molecule imaging via DNA-PAINT to directly compare the nanostructural organization of excitatory synapses forming onto PV-INs vs. onto excitatory neurons. Our detailed nanostructural analysis indicates that both PSD-95 and Munc13-1 at excitatory synapses on PV-INs form NCs that are aligned across the synapse from one another, suggesting that the nanocolumn is a conserved organizational principle of excitatory synapses. This interpretation is suggested by repeated observations of synaptic protein NCs (15–20) and alignment (21, 22) in other synapses and systems, but our detailed comparison with identical analyses at high imaging resolutions provides direct support for this conclusion. Conservation of nanocolumn alignment emphasizes the idea that common structural mechanisms govern the establishment of synaptic strength and provide distinct means for plastic changes at single synapses (1, 41). Indeed, experimental disruption of synaptic cleft interactions perturbs alignment of receptors with release sites and rapidly reduces the strength of synaptic transmission (14, 40, 42), suggesting that CAMs play key roles in these

mechanisms. Interestingly, while PV-INs express a unique set of CAMs compared to excitatory neurons (32–34) and form synapses on the quite morphologically distinct dendritic shaft instead of the spine head, Ex→PV synapses still form nanocolumns, underscoring the robust nature of this architecture and suggesting that it may be widely conserved in vivo.

Despite the general conservation of nanostructural features, however, key characteristics of both PSD-95 and Munc13-1 distributions depended on the identity of the postsynaptic cell. These differences are summarized in Fig. 4*I*. PSDs in Ex→PV synapses were larger overall with the same number of NCs, as if they were "stretched" Ex→Ex PSDs. However, individual NCs were larger and denser at Ex→PV synapses. Formation of these larger, denser PSD-95 NCs in PV-INs could be driven by PSD-95 interactors not found in excitatory neurons, such as Btbd11 (43), which might alter scaffold organization. The unique pattern of PSD-95 is expected to alter the distribution and mobility of NMDA receptors (NMDARs) and AMPA receptors (AMPARs) within these synapses as they diffuse within and between scaffold NCs (44, 45), which may capture more receptors and position them near sites of release to yield stronger EPSCs at Ex→PV synapses (28, 30). Conversely, PV-INs express a unique complement of Ca^{2+}-permeable AMPARs and TARPs (35, 46, 47) that may also exert an instructive influence on scaffold organization. These differences in organizational properties between synapse types suggest that PSD-95 is susceptible to organizational influences of other proteins in the synapse. This is in some contrast to the idea that PSD-95 could be a dominant driver of PSD organization (48), potentially as a central player in the phase separation properties of many synaptic proteins examined in vitro (49). Further, at least in the visual cortex, PV-INs developmentally express another MAGUK, SAP97, at higher levels than principal cells, and SAP97-expressing PV-INs have different functional properties (50). While SAP97 nanostructure has not been studied, it recruits different AMPAR subunits than PSD-95 (51), and as different MAGUKs have unique nanostructure (52), it may provide an additional contribution to the functional outcomes of PV-IN postsynaptic nanostructure through their development. In a general sense, it seems likely that the unique combination of molecular players in particular synapses could produce distinct classes of subsynaptic protein organization, either through a cooperative phase separation mechanism or through direct binding interactions.

One clear outcome of our work is that the organization of Munc13-1 within the AZ differs by postsynaptic cell identity. This key protein regulates both the docking and functional priming of SVs at the presynaptic membrane (53–57), so its distribution within the AZ has important consequences for neurotransmitter release. Presuming the axons in the synapses we analyzed drew equally from any excitatory cell-type present in these cultures, these data suggest retrograde regulation of the number and properties of presynaptic Munc13-1 NCs by the postsynaptic cell. This idea is supported by anatomical measurements showing directly that synapses along the same axon can have different release properties depending on the target cell (58, 59), which could be supported by divergent Munc13-1 nanostructure. At the molecular level, it may be that distinct CAM expression in the postsynaptic targets of a given axon (32) instructs afferent organization by selecting for specific presynaptic interacting partners that differentially organize the AZ. Functional impacts of such a mechanism have been described, as release probability from CA1 neurons onto different interneuron types is influenced by postsynaptic expression of neuroligin-3 (29) or ELFN1 (28), and local postsynaptic translation downstream of ErbB4 specifies excitatory synapse formation onto PV neurons (60). Beyond synapse strength, Ex→PV synapses are more stable (31), and we speculate that augmented or specific CAM content could lead both to enhanced alignment and decreased synaptic turnover. While our data are consistent with a retrograde impact of postsynaptic cell type, it is important to note that the presynaptic terminal likely also contributes unique aspects to Ex→Ex vs. Ex→PV synapse structure, as for example, ErbB4 must bind to presynaptic Neuregulin 3 at least for synapse formation (61), and presynaptic Narp secretion can induce GluA4 recruitment to Ex→PV synapses, which could impact nanostructure, and does alter homeostatic scaling (62).

Munc13-1 was present at greater density at Ex→PV synapses by confocal, and DNA-PAINT revealed it was organized into more numerous and larger, but less dense, NCs (Fig. 3). The number of Munc13-1 NCs that we observe within an AZ correlates with the number of release sites (5), suggesting that these synapses accommodate more docked vesicles at steady state. Presuming the release probability per site within an AZ is equal (3, 5), this difference in nanostructure producing a larger physiological N is expected to lead to a stronger excitatory drive onto PV-INs. The size and density of Munc13-1 NCs identified by immunogold EM varies considerably between AZs of CA1 pyramidal cell→F-SIN synapses (3). Here, we extend this observation in finding that the organization of individual Munc13-1 NCs varies between excitatory synapses onto different cell types. However, whether changing properties within single Munc13-1 NCs affects functions in docking and priming remains an open question of intense interest. Though reducing Munc13 content by knockout alters both processes (53, 56), Karlocai et al. (3) argue that the high docked vesicle occupancy at release sites (5, 37) suggests that varying Munc13-1 content per release site may principally control release probability at these sites, consistent with a potential effect on vesicle priming (37). Our findings are also consistent with previous work that suggests that Schaffer collateral synapses onto CA1 interneurons have a high probability of release due, in part, to a larger readily releasable pool (39). Thus, it is tempting to speculate that the density of Munc13-1 within NCs may be linked with vesicle priming state, but what factors drive the change in Munc13-1 distribution, and the resulting impact on AZ and Ex→PV synapse function, remain to be determined.

The transsynaptic spatial relationship between Munc13-1 and PSD-95, while conserved, was quantitatively different between Ex→Ex and Ex→PV synapses. In general terms, the alignment was stronger in Ex→PV synapses as revealed by the cross-correlation. This is of interest, since in large synapses, some glutamate receptors will lie farther away from some release sites than in small synapses, thus experiencing a lower amplitude glutamate transient. The augmented correlation of release sites and receptor scaffolds we observe would counteract this and suggests that controlling protein organization within the synapse interior to regulate transsynaptic alignment may reflect an equalizing mechanism in synapse types of varying geometry. Certainly, the geometric differences between these two synapse types extend beyond synapse size, since Ex→PV synapses generally form on the dendritic shaft as opposed to on dendritic spines. This structural difference clearly results in less electrical compartmentalization (63) and could further influence synaptic nanostructure in a number of ways, though the nanoscale properties of shaft synapses have not been well explored. These synapses contain different NMDAR content than spine synapses, dependent on postsynaptic cell-type (63, 64), and we have found NMDARs likely contribute to transsynaptic alignment (65). On the other hand, the actin cytoskeleton, which participates in spine synapse subsynaptic organization (66, 67), is intimately associated with both types of PSDs, contains similar filament types, and is similarly dynamic (68). Spiny CA1 neuron synapses

also scale in strength with distance from soma (69), but we did not observe distance-dependence of the mean or variance of confocal-level synaptic properties in Ex→PV synapses (data not shown). We expect that the interplay of synapse geometry, with molecular and nanostructural factors at these different synapse types contributes to the diversity of their function within particular cellular contexts.

An unexpected and intriguing difference between synapses was the cross-enrichment offset of PSD-95 from Munc13-1 NCs. Further exploration of this offset with a detailed spatial analysis of alignment suggested that Ex→PV synapses as a population contained a wider distribution of nanocolumn subtypes than their Ex→Ex counterparts. One interpretation is that the larger PSDs with larger PSD-95 NCs in Ex→PV synapses could represent an expanded platform upon which CAMs can bind, thus enabling more variance in their positioning and, consequently, more variance in the positioning of presynaptic structures around regions of high local PSD-95 density. In this model, Ex→PV synapse Munc13-1 NCs would be assembled at generally more distributed points around PSD-95 NCs. This is supported by the peak-to-peak measurements, the shift in the Munc13-1 NC cross-enrichment, and the breadth of the peak in both the PSD-95 NC cross-enrichment and the Munc13-1 NC sliding window analysis (Fig. 4). Manipulating PSD-95 clustering directly via artificial oligomerization to determine the impact on nanocolumn heterogeneity may permit a direct test of this model. At the single-synapse level, both synapse types harbored diverse nanocolumn subtypes, with on average slightly less diversity within a single Ex→PV synapse. In addition, our finding that Munc13-1 NCs experience high local, transsynaptic heterogeneity in PSD-95 enrichment within a single synapse is excellent support for the idea that synapses harbor release sites with diverse transsynaptic organizations that may differentiate the postsynaptic effects following release from any given site.

The existence of nanocolumns that are more offset in Ex→PV synapses would predict a displacement of AMPARs away from sites of release, but the average lateral offset (~10 to 20 nm) is itself modest and not likely to be functionally impactful. (Note that we did not compare AMPAR distribution directly in these experiments since the subunit composition is not equal and it is currently not possible to determine subtypes in imaging experiments.) Nevertheless, the organization suggests several possible differences in the synaptic mechanisms which control receptor mobility and determine their positioning. The more abundant space between PSD-95 NCs in the relatively enlarged Ex→PV synapses (Fig. 2*I*) suggests that an AMPAR diffusing within a PV-IN PSD experiences more space without an aligned release site. Thus, mechanisms to keep AMPARs in a PSD-95 NC, once one is encountered, could be particularly critical for maintaining the efficacy of the Ex→PV synapse. Indeed, larger, denser PSD-95 NCs may "capture" diffusing AMPARs more readily through their TARP intermediates, especially since PV-INs predominately express stargazin/TARPγ2, which has a higher affinity for PSD-95 than the prevalent TARP in Ex→Ex synapses, TARPγ8 (47). Cleft interactions may play a role as well. Neuronal pentraxins expressed predominantly in PV-INs interact directly with the N-terminal domains of AMPARs (70) and bind to presynaptic neuronal pentraxin receptor (NPR) to help concentrate AMPARs (71, 72). An offset in Munc13-1 and PSD-95 alignment could thus physically reflect or accommodate the presence of NPR in the AZ within the nanocolumn, providing an additional interaction to increase AMPAR dwell time there. Analysis of AMPAR mobility in these cell types following manipulation of either neuronal pentraxins or TARP content may help resolve these mechanisms. In a general sense, the goal of a synapse is to accumulate and stabilize receptors near neurotransmitter release sites, and the density pattern of PSD-95 will determine how receptors are handled in these two synapse types. This might be particularly impactful in PV-INs, where the dendritic shaft may not impose the same constraints to synapse size and receptor mobility as the membrane structure and bending of a dendritic spine.

Our most general conclusion is that rules of nanodomain assembly—arising from cell-type specific expression patterns—will elaborate synapse functional diversity. Expanding the analyses here to other Ex→IN synapse types will be instructive in efforts to understand this diversity. Note that presynaptic protein organization can be seen independently to influence synaptic strength by establishing the number of release sites, release probability, and features of facilitation and depression of release rate during sustained activity, whereas postsynaptic organization affects strength via controlling the mean number and type of receptors to be activated. Critically, transsynaptic nanoalignment integrates both these influences (9), helping to determine the resultant amplitude distribution during basal activity but also creating a higher-order impact on frequency-dependent information transfer properties. Thus, defining the nanostructural features and relationships among AZ, cleft, and PSD proteins will be essential for relating expression profiles and ultrastructure to functional diversity across the brain.

Materials and Methods

Detailed descriptions of *DNA Constructs, Lentivirus and Antibody Preparation, Primary Neuron Culture, Immunostaining, Microscopy, Image Analysis, and Statistics* can be found in *SI Appendix, Materials and Methods*.

DNA Constructs and Lentivirus Production. pFCaGW is a lentiviral vector that expresses EGFP (G) under the CaMKII promoter (Ca). psPAX2 (Addgene plasmid #12260; http://n2t.net/addgene:12260; RRID:Addgene_12260) and pMD2.G (Addgene plasmid #12259; http://n2t.net/addgene:12259; RRID:Addgene_12259) were gifts from Didier Trono. Lentivirus was produced in HEK293T cells transfected with 6 μg pFCaGW, 4 μg psPAX2, and 2 μg pMD2.G plus polyethylenimine. Virus-containing medium was harvested 48 h after transfection, centrifuged and filtered to remove debris, and stored in single-use aliquots at −80 °C.

Primary Culture. All animal procedures were approved by the University of Maryland Animal Use and Care committee. Dissociated primary hippocampal neuron cultures were prepared from E18 Sprague–Dawley rat embryos (Charles River) of both sexes as previously described (14) and plated on poly-L-lysine-coated coverslips at 30,000 cells/coverslip. Neurons were infected with 50 μL pFCaGW lentivirus at DIV5 and fixed at DIV21 for both confocal and DNA-PAINT experiments.

Immunostaining. pFCaGW-infected or naive neurons were fixed with 2% paraformaldehyde + 4% sucrose in PBS for 10 min at room temperature (RT), washed, permeabilized with 0.3% Triton X-100 for 20 min, and blocked with 10% donkey serum + 0.2% Triton X-100. For confocal imaging, neurons were incubated overnight at 4 °C with primary antibodies toward PSD-95, Munc13-1, and either GFP (for pFCaGW-infected cells) or PV (for naive cells). The next day, cells were washed and incubated with secondary antibodies for 1 h at RT, washed again, and postfixed. For DNA-PAINT, the PSD-95 and Munc13-1 primary antibodies were separately preincubated with single-domain antibodies (Massive Photonics) carrying orthogonal oligonucleotides for DNA-PAINT for 20 min at RT, then mixed with either anti-EGFP or anti-PV, and incubated on the sample overnight at 4 °C. The next day, Alexa 488–conjugated secondary antibodies toward anti-EGFP and anti-PV were applied as above, followed by postfixation.

Microscopy. Confocal images were acquired on a Nikon TI2 Eclipse inverted microscope with a Nikon Apo TIRF 60×/1.49 NA objective, a Dragonfly confocal unit (Andor), and a Zyla4.2 sCMOS camera (Andor). 3D DNA-PAINT images were

acquired on a custom microscope built around an RM21 base (Mad City labs) with an Olympus UPlanApo60x OHR/1.5 NA objective and a Prime95b sCMOS camera (Photometrics). Both systems yielded pixel sizes of 100 nm.

Confocal and DNA-PAINT Analysis. Confocal images were analyzed with a custom ImageJ macro based on puncta detection by the SynQuant plugin (32). DNA-PAINT acquisitions were analyzed in 3D, similar to ref. 10. See *SI Appendix, Materials and Methods*, for detailed explanations of analysis methods.

Statistics. Statistical analyses were performed in GraphPad PRISM. Data were tested for normality, and data that passed this check were tested for statistical differences with two-tailed *t* test if variance was equal between groups, or Welch's *t* test if not, or with two-way ANOVA followed by post hoc Šidák multiple comparison tests where appropriate. Data that did not pass the normality check were tested with two-tailed Mann–Whitney tests.

Data, Materials, and Software Availability. Data from this paper have been deposited in the Open Science Framework at https://osf.io/ex7sz (73). Source code for the analyses has been made available at https://github.com/blanpiedlab/DharmasriLevy-PNAS-2024 (74).

ACKNOWLEDGMENTS. This work was supported by F31 MH117920 and T32 GM008181 to P.A.D., F32 MH119687 to A.D.L, and R37 MH080046 and R01 MH119826 to T.A.B. We thank the members of the Blanpied Laboratory for rigorous discussion and critical evaluation of the manuscript and Minerva Contreras for technical assistance.

Author affiliations: [a]Department of Physiology, University of Maryland School of Medicine, Baltimore, MD 21201; [b]Program in Neuroscience, University of Maryland School of Medicine, Baltimore, MD 21201; and [c]University of Maryland-Medicine Institute of Neuroscience Discovery, University of Maryland School of Medicine, Baltimore, MD 21201

1. X.-Z. Gou, A. M. Ramsey, A.-H. Tang, Re-examination of the determinants of synaptic strength from the perspective of superresolution imaging. *Curr. Opin. Neurobiol.* **74**, 102540 (2022).
2. M. A. Böhme *et al.*, Active zone scaffolds differentially accumulate Unc13 isoforms to tune Ca2+ channel–vesicle coupling. *Nat. Neurosci.* **19**, 1311–1320 (2016).
3. M. R. Karlocai *et al.*, Variability in the Munc13-1 content of excitatory release sites. *eLife* **10**, e67468 (2021).
4. N. Rebola *et al.*, Distinct nanoscale calcium channel and synaptic vesicle topographies contribute to the diversity of synaptic function. *Neuron* **104**, 693–710.e9 (2019).
5. H. Sakamoto *et al.*, Synaptic weight set by Munc13-1 supramolecular assemblies. *Nat. Neurosci.* **21**, 41–49 (2018).
6. Y. Fukata *et al.*, Local palmitoylation cycles define activity-regulated postsynaptic subdomains. *J. Cell Biol.* **202**, 145–161 (2013).
7. H. D. MacGillavry, Y. Song, S. Raghavachari, T. A. Blanpied, Nanoscale scaffolding domains within the postsynaptic density concentrate synaptic AMPA receptors. *Neuron* **78**, 615–622 (2013).
8. D. Nair *et al.*, Super-resolution imaging reveals that AMPA receptors inside synapses are dynamically organized in nanodomains regulated by PSD95. *J. Neurosci.* **33**, 13204–13224 (2013).
9. T. Biederer, P. S. Kaeser, T. A. Blanpied, Transcellular nanoalignment of synaptic function. *Neuron* **96**, 680–696 (2017).
10. A.-H. Tang *et al.*, A trans-synaptic nanocolumn aligns neurotransmitter release to receptors. *Nature* **536**, 210 (2016).
11. X. Li, G. Hémond, A. G. Godin, N. Doyon, Computational modeling of trans-synaptic nanocolumns, a modulator of synaptic transmission. *Front. Comput. Neurosci.* **16**, 969119 (2022).
12. L. P. Savtchenko, D. A. Rusakov, Moderate AMPA receptor clustering on the nanoscale can efficiently potentiate synaptic current. *Philos. Trans. R. Soc. Lond. B. Biol. Sci.* **369**, 20130167 (2014).
13. X. Xie, J.-S. Liaw, M. Baudry, T. W. Berger, Novel expression mechanism for synaptic potentiation: Alignment of presynaptic release site and postsynaptic receptor. *Proc. Natl. Acad. Sci. U.S.A.* **94**, 6983–6988 (1997).
14. A. M. Ramsey *et al.*, Subsynaptic positioning of AMPARs by LRRTM2 controls synaptic strength. *Sci. Adv.* **7**, eabf3126 (2021).
15. M. J. Broadhead *et al.*, PSD95 nanoclusters are postsynaptic building blocks in hippocampus circuits. *Sci. Rep.* **6**, 24626 (2016).
16. V. Clavet-Fournier *et al.*, Pre- and postsynaptic nanostructures increase in size and complexity after induction of long-term potentiation. *iScience* **27**, 108679 (2024).
17. A. Martinez-Sanchez *et al.*, Trans-synaptic assemblies link synaptic vesicles and neuroreceptors. *Sci. Adv.* **7**, eabe6204 (2021).
18. D. Sarkar *et al.*, Revealing nanostructures in brain tissue via protein decrowding by iterative expansion microscopy. *Nat. Biomed. Eng.* **6**, 1057–1073 (2022).
19. S.-Y. Sun *et al.*, Correlative assembly of subsynaptic nanoscale organizations during development. *Front. Synaptic Neurosci.* **14**, 748184 (2022).
20. W. Wegner, A. C. Mott, S. G. N. Grant, H. Steffens, K. I. Willig, In vivo STED microscopy visualizes PSD95 sub-structures and morphological changes over several hours in the mouse visual cortex. *Sci. Rep.* **8**, 219 (2018).
21. P. Muttathukunnel, P. Frei, S. Perry, D. Dickman, M. Müller, Rapid homeostatic modulation of transsynaptic nanocolumn rings. *Proc. Natl. Acad. Sci. U.S.A.* **119**, e2119044119 (2022).
22. K. C. Crosby *et al.*, Nanoscale subsynaptic domains underlie the organization of the inhibitory synapse. *Cell Rep.* **26**, 3284–3297.e3 (2019).
23. M. Niu *et al.*, Droplet-based transcriptome profiling of individual synapses. *Nat. Biotechnol.* **41**, 1332–1344 (2023).
24. Z. Yao *et al.*, A high-resolution transcriptomic and spatial atlas of cell types in the whole mouse brain. *Nature* **624**, 317–332 (2023).
25. E. Favuzzi, B. Rico, Molecular diversity underlying cortical excitatory and inhibitory synapse development. *Curr. Opin. Neurobiol.* **53**, 8–15 (2018).
26. G. Gonzalez-Burgos, D. A. Lewis, NMDA receptor hypofunction, parvalbumin-positive neurons, and cortical gamma oscillations in Schizophrenia. *Schizophr. Bull.* **38**, 950–957 (2012).
27. O. Marín, Interneuron dysfunction in psychiatric disorders. *Nat. Rev. Neurosci.* **13**, 107–120 (2012).
28. E. L. Sylwestrak, A. Ghosh, Elfn1 regulates target-specific release probability at CA1–interneuron synapses. *Science* **338**, 536–540 (2012).
29. J. S. Polepalli *et al.*, Modulation of excitation on parvalbumin interneurons by neuroligin-3 regulates the hippocampal network. *Nat. Neurosci.* **20**, 219–229 (2017).
30. N. V. Povysheva *et al.*, Properties of excitatory synaptic responses in fast-spiking interneurons and pyramidal cells from monkey and rat prefrontal cortex. *Cereb. Cortex* **16**, 541–552 (2006).
31. J. B. Melander *et al.*, Distinct in vivo dynamics of excitatory synapses onto cortical pyramidal neurons and parvalbumin-positive interneurons. *Cell Rep.* **37**, 109972 (2021).
32. C. Földy *et al.*, Single-cell RNAseq reveals cell adhesion molecule profiles in electrophysiologically defined neurons. *Proc. Natl. Acad. Sci. U.S.A.* **113**, E5222–E5231 (2016).
33. A. Paul *et al.*, Transcriptional architecture of synaptic communication delineates GABAergic neuron identity. *Cell* **171**, 522–539.e20 (2017).
34. L. Que, D. Lukacsovich, W. Luo, C. Földy, Transcriptional and morphological profiling of parvalbumin interneuron subpopulations in the mouse hippocampus. *Nat. Commun.* **12**, 108 (2021).
35. K. A. Pelkey *et al.*, Hippocampal GABAergic inhibitory interneurons. *Physiol. Rev.* **97**, 1619–1747 (2017).
36. Y. Wang *et al.*, SynQuant: An automatic tool to quantify synapses from microscopy images. *Bioinformatics* **36**, 1599–1606 (2020).
37. M. Aldahabi *et al.*, Different priming states of synaptic vesicles underlie distinct release probabilities at hippocampal excitatory synapses. *Neuron* **110**, 4144–4161.e7 (2022).
38. A. B. Ali, J. Deuchars, H. Pawelzik, A. M. Thomson, CA1 pyramidal to basket and bistratified cell EPSPs: Dual intracellular recordings in rat hippocampal slices. *J. Physiol.* **507**, 201–217 (1998).
39. H. Y. Sun, S. A. Lyons, L. E. Dobrunz, Mechanisms of target-cell specific short-term plasticity at Schaffer collateral synapses onto interneurones versus pyramidal cells in juvenile rats. *J. Physiol.* **568**, 815–840 (2005).
40. K. T. Haas *et al.*, Pre-post synaptic alignment through neuroligin-1 tunes synaptic transmission efficiency. *eLife* **7**, e31755 (2018).
41. H. Chen, A.-H. Tang, T. A. Blanpied, Subsynaptic spatial organization as a regulator of synaptic strength and plasticity. *Curr. Opin. Neurobiol.* **51**, 147–153 (2018).
42. Y. Fukata *et al.*, LGI1–ADAM22–MAGUK configures transsynaptic nanoalignment for synaptic transmission and epilepsy prevention. *Proc. Natl. Acad. Sci. U.S.A.* **118**, e2022580118 (2021).
43. A. M. Bygrave *et al.*, Btbd11 supports cell-type-specific synaptic function. *Cell Rep.* **42**, 112591 (2023).
44. T. P. Li, T. A. Blanpied, Control of transmembrane protein diffusion within the postsynaptic density assessed by simultaneous single-molecule tracking and localization microscopy. *Front. Synaptic Neurosci.* **8**, 19 (2016).
45. T. P. Li, Y. Song, H. D. MacGillavry, T. A. Blanpied, S. Raghavachari, Protein crowding within the postsynaptic density can impede the escape of membrane proteins. *J. Neurosci.* **36**, 4276–4295 (2016).
46. M. Yamasaki *et al.*, TARP γ-2 and γ-8 differentially control AMPAR density across schaffer collateral/commissural synapses in the hippocampal CA1 area. *J. Neurosci.* **36**, 4296–4312 (2016).
47. M. Zeng *et al.*, Phase separation–mediated TARP/MAGUK complex condensation and AMPA receptor synaptic transmission. *Neuron* **104**, 529–543.e6 (2019).
48. Y. Hayashi, L. K. Ford, L. Fioriti, L. McGurk, M. Zhang, Liquid-liquid phase separation in physiology and pathophysiology of the nervous system. *J. Neurosci.* **41**, 834–844 (2021).
49. M. Zeng *et al.*, Reconstituted postsynaptic density as a molecular platform for understanding synapse formation and plasticity. *Cell* **174**, 1172–1187.e16 (2018).
50. G. Akgul, L. P. Wollmuth, Synapse-associated protein 97 regulates the membrane properties of fast-spiking parvalbumin interneurons in the visual cortex. *J. Neurosci.* **33**, 12739–12750 (2013).
51. A. S. Leonard, M. A. Davare, M. C. Horne, C. C. Garner, J. W. Hell, SAP97 is associated with the α-Amino-3-hydroxy-5-methylisoxazole-4-propionic acid receptor GluR1 subunit. *J. Biol. Chem.* **273**, 19518–19524 (1998).
52. S. R. Metzbower, P. A. Dharmasri, A. D. Levy, M. C. Anderson, T. A. Blanpied, Distinct SAP102 and PSD-95 nano-organization defines multiple types of synaptic scaffold protein domains at single synapses. bioRxiv [Preprint] (2023). https://doi.org/10.1101/2023.09.12.557372 (Accessed 5 October 2023).
53. A. T. Brunger, U. B. Choi, Y. Lai, J. Leitz, Q. Zhou, Molecular mechanisms of fast neurotransmitter release. *Annu. Rev. Biophys.* **47**, 469–497 (2018).
54. P. S. Kaeser, W. G. Regehr, The readily releasable pool of synaptic vesicles. *Curr. Opin. Neurobiol.* **43**, 63–70 (2017).
55. J. Rizo, Mechanism of neurotransmitter release coming into focus. *Protein Sci.* **27**, 1364–1391 (2018).
56. C. Tan *et al.*, Munc13 supports fusogenicity of non-docked vesicles at synapses with disrupted active zones. *eLife* **11**, e79077 (2022).
57. C. Tan, S. S. H. Wang, G. de Nola, P. S. Kaeser, Rebuilding essential active zone functions within a synapse. *Neuron* **110**, 1498–1515.e8 (2022).
58. H. Markram, Y. Wang, M. Tsodyks, Differential signaling via the same axon of neocortical pyramidal neurons. *Proc. Natl. Acad. Sci. U.S.A.* **95**, 5323–5328 (1998).
59. H. J. Koester, D. Johnston, Target cell-dependent normalization of transmitter release at neocortical synapses. *Science* **308**, 863–866 (2005).
60. C. Bernard *et al.*, Cortical wiring by synapse type–specific control of local protein synthesis. *Science* **378**, eabm7466 (2022).
61. T. Müller *et al.*, Neuregulin 3 promotes excitatory synapse formation on hippocampal interneurons. *EMBO J.* **37**, e98858 (2018).
62. M. C. Chang *et al.*, Narp regulates homeostatic scaling of excitatory synapses on parvalbumin-expressing interneurons. *Nat. Neurosci.* **13**, 1090–1097 (2010).

63. L. Sancho, B. L. Bloodgood, Functional distinctions between spine and dendritic synapses made onto parvalbumin-positive interneurons in mouse cortex. *Cell Rep.* **24**, 2075–2087 (2018).
64. C. Xu *et al.*, Structure and plasticity of silent synapses in developing hippocampal neurons visualized by super-resolution imaging. *Cell Discov.* **6**, 8 (2020).
65. P. A. Dharmasri, E. M. DeMarco, M. C. Anderson, A. D. Levy, T. A. Blanpied, Loss of postsynaptic NMDARs drives nanoscale reorganization of Munc13-1 and PSD-95. bioRxiv [Preprint] (2024). https://doi.org/10.1101/2024.01.12.574705 (Accessed 15 February 2024).
66. J. M. Kerr, T. A. Blanpied, Subsynaptic AMPA receptor distribution is acutely regulated by actin-driven reorganization of the postsynaptic density. *J. Neurosci.* **32**, 658–673 (2012).
67. H. D. MacGillavry, J. M. Kerr, J. Kassner, N. A. Frost, T. A. Blanpied, Shank-cortactin interactions control actin dynamics to maintain flexibility of neuronal spines and synapses. *Eur. J. Neurosci.* **43**, 179–193 (2016).
68. B. Van Bommel, A. Konietzny, O. Kobler, J. Bär, M. Mikhaylova, F-actin patches associated with glutamatergic synapses control positioning of dendritic lysosomes. *EMBO J.* **38**, e101183 (2019).
69. T. E. Chater, Y. Goda, The shaping of AMPA receptor surface distribution by neuronal activity. *Front. Synaptic Neurosci.* **14**, 833782 (2022).
70. K. A. Pelkey *et al.*, Pentraxins coordinate excitatory synapse maturation and circuit integration of parvalbumin interneurons. *Neuron* **85**, 1257–1272 (2015).
71. S.-J. Lee *et al.*, Presynaptic neuronal pentraxin receptor organizes excitatory and inhibitory synapses. *J. Neurosci.* **37**, 1062–1080 (2017).
72. G.-M. Sia *et al.*, Interaction of the N-terminal domain of the AMPA receptor GluR4 subunit with the neuronal pentraxin NP1 mediates GluR4 synaptic recruitment. *Neuron* **55**, 87–102 (2007).
73. P. A. Dharmasri, A. D. Levy, T. A. Blanpied, Data from "Differential nanoscale organization of excitatory synapses onto excitatory vs. inhibitory neurons." Open Science Framework. https://osf.io/ex7sz. Deposited 3 April 2024.
74. P. A. Dharmasri, A. D. Levy, T. A. Blanpied, Code for "Differential nanoscale organization of excitatory synapses onto excitatory vs. inhibitory neurons." GitHub.com. https://github.com/blanpiedlab/DharmasriLevy-PNAS-2024. Deposited 3 April 2024.